*aerospace*

MDPI

*Article*

# Prediction of Spectral Response for Explosion Separation Based on DeepONet

**Xiaoqi Chen [1], Zhanlong Qu [2], Yuxi Wang [3,4], Zihao Chen [3,4,*], Ganchao Chen [3,4,*], Xiao Kang [3,4] and Ying Li [3,4]**

[1] School of Naval Architecture, Ocean and Energy Power Engineering, Wuhan University of Technology, Wuhan 430064, China
[2] China Academy of Launch Vehicle Technology, Beijing 100076, China
[3] Institute of Advanced Structure Technology, Beijing Institute of Technology, Beijing 100081, China; xiao.kang@bit.edu.cn (X.K.)
[4] State Key Laboratory of Explosion Science and Technology, Beijing Institute of Technology, Beijing 100081, China
* Correspondence: chenzihao1993@gmail.com (Z.C.); chenganchao@bit.edu.cn (G.C.)

**Abstract:** Strong shock waves generated during the pyrotechnic separation process of aerospace vehicles can cause high-frequency damage or even structural failure to the vehicle's structure. Existing structural designs for shock attenuation typically rely on shock response spectra methods, which require multiple finite element calculations to determine the optimal geometric parameters, leading to relatively low efficiency. In this work, we propose a spectral response prediction method for spacecraft structures using the Deep Operator Network (DeepONet). This method preserves the physical relationships between input variables, modularizes geometric and positional input data, and outputs the spectral response. We integrate this neural model to analyze the impact of spacecraft structural parameters on shock resistance performance, revealing that circumferential reinforcement has the most significant influence on shock resistance. Then, we conduct a detailed analysis of the DeepONet model, noting that models with a higher number of neurons per layer train more quickly but are prone to overfitting. Additionally, we find that focusing on specific frequency bands for spectral response prediction yields more accurate results.

**Keywords:** explosive separation; DeepONet; frequency domain machine learning; neural network analysis

check for updates

Academic Editor: Bo Zhang

Received: 27 February 2025
Revised: 28 March 2025
Accepted: 2 April 2025
Published: 4 April 2025

**Citation:** Chen, X.; Qu, Z.; Wang, Y.; Chen, Z.; Chen, G.; Kang, X.; Li, Y. Prediction of Spectral Response for Explosion Separation Based on DeepONet. *Aerospace* **2025**, *12*, 310. https://doi.org/10.3390/aerospace12040310

**Copyright:** © 2025 by the authors. Licensee MDPI, Basel, Switzerland. This article is an open access article distributed under the terms and conditions of the Creative Commons Attribution (CC BY) license (https://creativecommons.org/licenses/by/4.0/).

## 1. Introduction

During the launch process of multi-stage spacecraft, interstage separation is typically required at a predetermined position between adjacent stages to improve the flight characteristics of the vehicle. Due to its simple structure and fast action, the pyrotechnic separation device is widely used in spacecraft separation tasks [1,2]. The pyrotechnic separation device ensures reliable chamber connection and, at a predetermined position, triggers internal explosives that release high-pressure gas to cut the connecting parts, completing the separation task. However, the shock waves generated during the explosive separation process create localized high-frequency (100–100,000 Hz), transient (with amplitude decaying to 10% of the peak acceleration within 20 ms), and high-amplitude (4000–100,000 g) shock responses on the spacecraft structure, known as the explosive shock environment. This can easily cause damage to the related instruments and equipment [3].

At the same time, the spacecraft structure is a typical stiffened plate structure. To withstand the harsh explosive shock environment, it is usually iteratively optimized during

the design phase using numerical methods to obtain the best shock resistance parameters. This, however, leads to expensive computational costs and long development cycles. Therefore, developing more efficient computational methods is of significant practical importance [4,5].

In recent years, machine learning has become a new paradigm for mechanical calculations [6–8]. By learning from large datasets, they train a set of parameters to establish the mapping relationship between input and output data. These methods have been widely applied in fields such as vehicle collisions [9], ship damage [10,11], high-energy material damage [12], and structure design [13]. However, traditional machine learning methods are akin to a 'black box' and may provide predictions that violate physical constraints. As a result, some scholars have attempted to impose certain physical constraints on machine learning [14]. For instance, a Physics-Informed Neural Network (PINN) method combines physical partial differential equations (PDEs) with neural networks [15,16], allowing for predictions that satisfy physical constraints even with small sample sizes [17,18]. However, this method, while imposing complete physical constraints, also limits a PINN to handle only one operating condition at a time [17]. Therefore, some scholars have sought to extend the capabilities of PINNs to predict a range of problems [19,20]. DeepONet, proposed in [21], aims to achieve function-to-function mapping by learning physical operators. Its unique two-part neural network structure, called the branch network and trunk network, modularizes the inputs and performs pointwise multiplication projections, preserving the physical relationships between the relevant variables. This approach has shown promising predictive performance in various areas, including hypersonic flow [22], crack propagation [23], and microstructural topology optimization [24].

At the same time, some researchers have extended the DeepONet method to achieve enhanced learning capabilities [25–27]. The earlier version of DeepONet, which only aggregates the outputs of the trunk and branch networks through a dot product operation, might lead to insufficient information fusion [26]. Subsequent improvements include earlier information fusion and enhanced fusion complexity [27]. Another similar method proposed in [28] shares a neural network structure very similar to DeepONet. The key difference is that it does not strictly separate the branch and trunk networks but instead uses several neural networks to learn groups of input variables based on their physical similarities. A single neural network is used to combine all the data and provide final prediction.

At the same time, when training the neural network, it is important to consider the specificity of the explosive separation spectral response problem [29]. That is, the time-domain acceleration response curve of the explosive separation shock wave exhibits a complex oscillatory waveform that is difficult to analyze [30]. Related analyses are typically conducted in the frequency domain—by using Fourier transforms to convert the time-domain response into a frequency-domain response and analyzing the maximum acceleration response amplitude at each natural frequency [30,31]. This is referred to as the shock response spectrum method. Therefore, in the explosive separation problem, the model being developed is essentially a surrogate model for predicting the spectral acceleration response, which is a frequency-domain machine learning approach.

Theoretically, time-domain data can be converted into frequency-domain data corresponding to natural frequencies ranging from 1 Hz to infinity. However, in practice, the transformation process inevitably omits certain frequency bands [20]. Some studies also suggest that when training machine learning models in the frequency domain, selectively omitting some frequency bands may lead to better prediction results [32]. Some researchers choose to omit certain noise frequency bands in their work [20]. However, beyond the noise frequency bands, the impact of the range of the data frequency band on prediction results still requires further investigation.

This paper aims to develop a fast prediction model for spacecraft structure spectral response. First, a finite element model of the spacecraft explosion separation process is established to analyze the structural response and provide spectral response characteristic curves at relevant locations in the frequency domain. Next, DeepONet is used to establish the mapping relationship between the cabin geometry and the corresponding maximum spectral acceleration response amplitude. The neural network model is combined to analyze the impact of cabin geometric parameters on the spectral acceleration response amplitude. Finally, we investigate the impact of the data frequency band range on the prediction results within the frequency-domain machine learning model for explosive separation.

## 2. Numerical Model of Explosive Separation

### *2.1. Problem Description of Explosive Separation*

The spacecraft cabin structure is a stiffened plate structure, with adjacent cabins connected by flexible detonation cords, as shown in Figure 1. Upon reaching a predetermined position, the explosive inside the detonation cord is triggered, and the high-energy gas released cuts the weak section of the detonation cord, unlocking and separating the adjacent cabins. The harsh shock environment generated by this explosive separation process is referred to as the explosive separation shock environment, which is primarily characterized by high-frequency, high-amplitude acceleration responses. Relevant analyses are also conducted based on the maximum acceleration response.

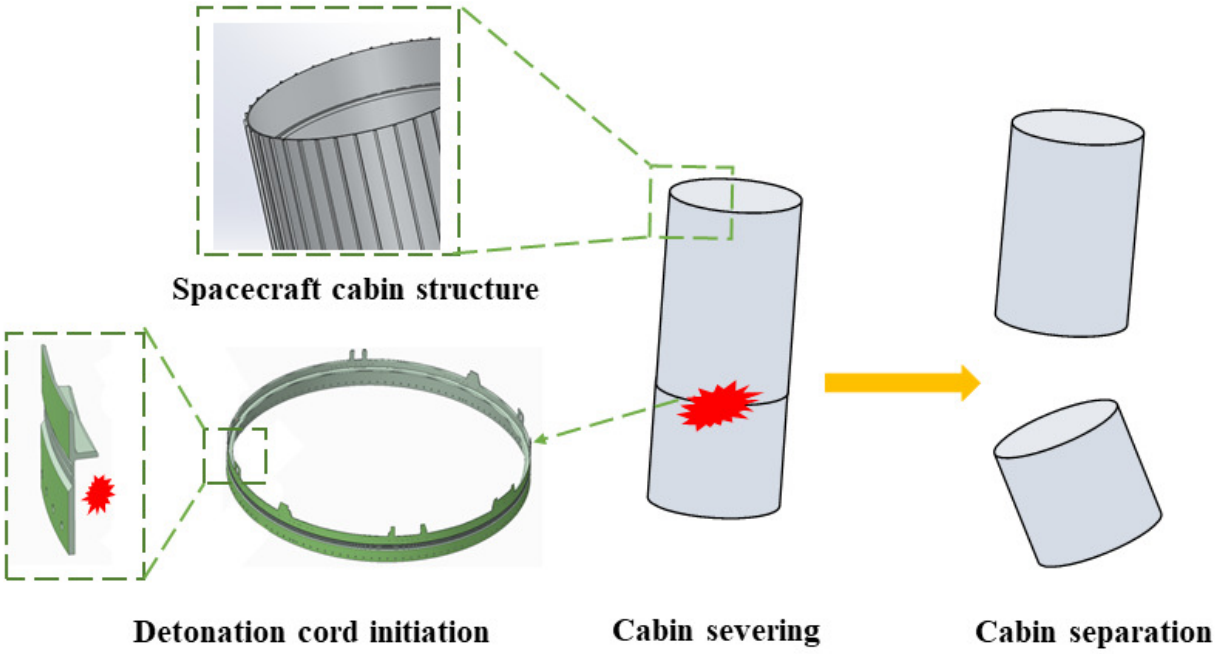



**Figure 1.** Schematic diagram of explosive separation.

### *2.2. Finite Element Model*

The spacecraft cabin structure consists of a stiffened cylindrical design, as shown in Figure 2a, comprising a bulkhead, internal reinforcements, and external reinforcements. The bulkhead has a length of $l$ = 4200 mm, a diameter of $d$ = 5000 mm, and a thickness of $T$ = 15 mm. The internal reinforcement has a parameter of $r_1$ = 80 mm, while the external reinforcement plate thickness is $r_2$ = 16 mm. The detonation cord is positioned at the connection point of the cabin structure, as shown in Figure 2b.

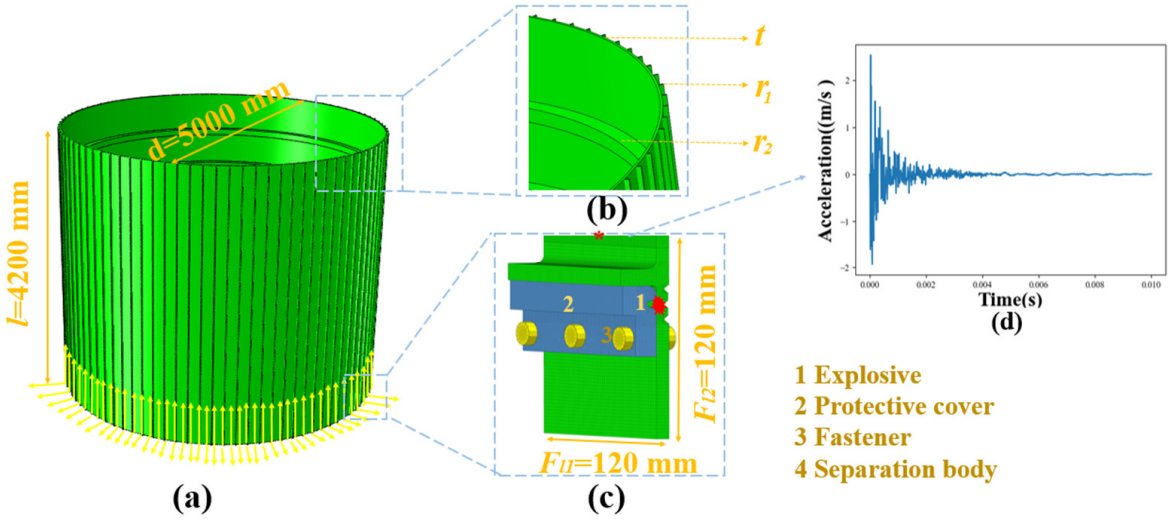



**Figure 2.** Finite element model of explosive separation: (**a**) Spacecraft cabin structure. (**b**) Geometry of the detonation cord. (**c**) Finite element model of the detonation cord. (**d**) Explosion response of detonation cord which also is the input loading of cabin structure.

Except for explosives, both the detonation cord structure and the cabin structure are made of aluminum alloy, and its constitutive relationship is represented by Equation (1):

$$\sigma_y = \sigma_{y0} + E_h \bar{\varepsilon}_p \tag{1}$$

where $\sigma_y$ and $\sigma_{y0}$ are the yield stress and initial yield stress, respectively, $\bar{\varepsilon}_p$ is the equivalent plastic strain, and $E_h$ is the plastic hardening modulus. The thermodynamic state of the aluminum alloy is described using the Gruneisen equation of state. The pressure $P$ (positive in compression) is determined by Equations (2) and (3), which represent the equation of state in the loaded and unloaded states, respectively.

$$P = \rho_0 C^2 \mu + (\gamma_0 + a\mu)U, \quad \mu \leq 0 \tag{2}$$

$$P = \frac{\rho_0 C^2 \mu [1 + (1 - \frac{\gamma_0}{2})\mu - \frac{a}{2}\mu^2]}{[1 - (S_1 - 1)\mu - S_2 \frac{\mu^2}{\mu+1} - S_3 \frac{\mu^3}{(\mu+1)^2}]^2} + (\gamma_0 + a\mu)U, \quad \mu \geq 0 \tag{3}$$

$$\mu = \rho/\rho_0 - 1 \tag{4}$$

where $\rho_0$ and $\rho$ represent the material's initial and current densities, respectively, while $\mu$ quantifies the material's compression level. $\gamma_0$ is the Gruneisen coefficient, and $a$ is the first-order correction term for the Gruneisen coefficient, typically assumed to be zero; $U$ corresponds to the internal energy. The parameters $S_1$, $S_2$, $S_3$, and $C$ are obtained from the impact adiabatic curve which is defined as

$$D = C + S_1 v + S_2 v^2 + S_3 v^3 \tag{5}$$

where $D$ is the shock wave velocity, and $v$ is the particle velocity; Equation (5) is used to determine the correlation coefficient by describing the relationship between the two. It can also be used to describe the shock wave propagation process. The material parameters for the aluminum alloy, including density, elastic modulus, shear modulus, Poisson's ratio, yield strength, plastic hardening modulus, and other parameters referenced in Equations (2), (3), and (5), are summarized in Table 1.

**Table 1.** Material parameters for the aluminum alloy.

| $\rho$ (kg/m$^3$) | $E$ (GPa) | $G$ (GPa) | $v$ | $\sigma_{y0}$ (MPa) | $E_h$ (MPa) | $\gamma_0$ | $C$ (m/s) | $S_1$ | $S_2$ | $S_3$ |
|---|---|---|---|---|---|---|---|---|---|---|
| 2785 | 71 | 26.5 | 0.32 | 350 | 777 | 2.77 | 4080 | 1.86 | 0 | 0 |

The separation cabin structure is connected by a detonation cord. Considering that the detonation cord model has a segmented cyclic symmetric structure, a characteristic segment with a length of 120 mm, as shown in Figure 2c, is selected for finite element analysis. The model is composed of explosives, protective cover, connecting fasteners, and separated shells. Specifically, the explosive material used is RDX, and the JWL equation of state is employed to simulate its blast capacity:

$$P = A\left(1 - \frac{\omega}{R_1 V}\right)e^{-R_1 V} + B\left(1 - \frac{\omega}{R_2 V}\right)e^{-R_2 V} + \frac{\omega U}{V} \tag{6}$$

where $P$ is the pressure of the detonation products, $V$ is the relative volume, and $U$ is the internal energy per unit volume. $A$, $B$, $R_1$, $R_2$, and $\omega$ are the energy-containing explosives equation inherent parameters, with their values provided in Table 2.

**Table 2.** JWL parameters for RDX.

| $\rho$ (kg/m$^3$) | $D$ (m/s) | $U$ (MJ/kg) | $A$ (GPa) | $B$ (GPa) | $R_1$ | $R_2$ | $\omega$ |
|---|---|---|---|---|---|---|---|
| 1670 | 7420 | 6.53 | 611.3 | 10.65 | 4.4 | 1.2 | 0.32 |

Considering the high computational cost of the entire detonation cord–cabin explosive separation model, and the fact that the detonation cord response, after being isolated by the protective cover, is primarily transmitted along the separation body to the adjacent cabin structure, the detonation cord model shown in Figure 2c is calculated independently. The acceleration response at the connection between the detonation cord and the cabin wall is obtained, as shown in Figure 2d, and is used as the input load for the cabin wall section shown in Figure 2a.

The dynamic response of the cabin wall structure under this loading can be described by the momentum conservation equation, which governs the relationship between the applied load and the resulting structural acceleration. Its three-dimensional form is given as follows:

$$\frac{\sigma_{ij}}{x_j} + \rho b_i = \rho \frac{\partial^2 u_i}{\partial t^2} \tag{7}$$

where $\sigma_{ij}$ denotes the components of the stress tensor, $x_j$ represents the spatial coordinate axes, $\rho$ is the material density, $b_i$ is the body force component, and $u_i$ is the displacement component in the $i$-th direction.

Grid generation was completed using HyperMesh 2022 software. The mesh sizes for the spacecraft cabin structure, separation body, explosive material, protective cover, and fasteners are set to 5 mm, 0.6 mm, 2 mm, 1 mm, 2 mm, and 5 mm, respectively, and the mesh size near the separation plate's weakening groove, where the explosive is located, is set to 0.7 mm. The Euler–Lagrange (CEL) algorithm was used for simulation. For the flexible detonation cord, Lagrangian elements were used, except for the explosive material, with Euler elements applied to the charge location to simulate the air and energetic explosive material. The theoretical charge amount for the flexible detonation cord is 4.2 g/m. The target charge mass was achieved by adjusting the volume occupied by the Euler elements

representing the energetic explosive material. Symmetric boundary conditions were set on both sides, and the analysis step time was set to 0.01 s. The entire model was set up with general contact. The final output of the structure includes the strain response and the acceleration response at measurement points located on the internal reinforcements, spaced 600 mm apart.

### *2.3. Finite Element Model Validation*

In our previous study, we investigated the effect of adding microstructures between the detonation cord and the bulkhead on the spectral response of the explosively separated bulkhead structure (see in Figure 3). The accuracy of the employed finite element model was validated through experiments. The finite element model used in this study is consistent with that of the previous work, and further details can be found in [29].

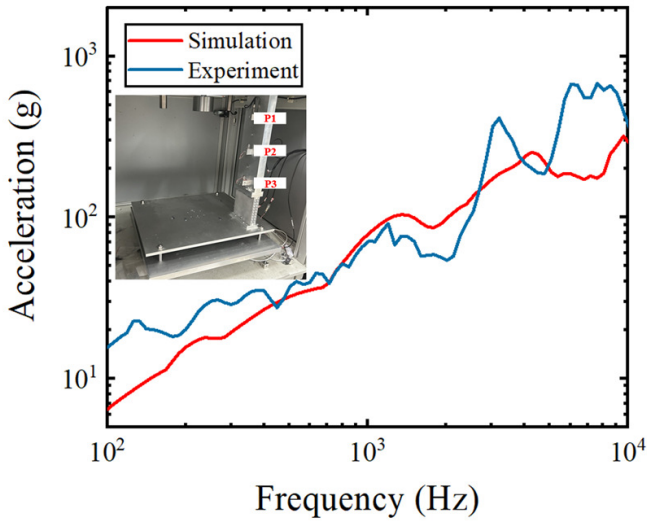



**Figure 3.** Finite element model validation.

## 3. Machine Learning Models

### *3.1. DeepONet*

DeepONet directly learns the mapping of an entire function space through its unique modular neural network structure. Specifically, in the case of spacecraft explosion separation discussed in this paper, since the amount of explosive material in the detonator cord is consistent, the differences between the calculation conditions lie solely in the structural geometric parameters. That is, when $T$, $r_1$, and $r_2$ are determined, the response of the entire structure is already fixed. In the real physical world, the mapping should be from the geometric structure space to the acceleration response space. We can only observe the structure's response from different locations, but the different observation points do not affect the overall response of the structure.

The neural network input is divided into two parts, as shown in Figure 4. One part expresses the input function space, known as the branch network. This corresponds to the geometric space that determines the final response (i.e., the geometric part in the diagram). The other part of the neural network, known as the trunk network, inputs the information used to query the final response, such as the position $X$ and frequency $f$ of the measurement points. The final prediction is made by combining the outputs of the two networks through a dot product summation in the intersection part of the network. It can be seen that for different sampling points on the same structure, when the geometry remains the same but the position changes, the neural network representing the structure's geometry remains

consistent. This modular approach allows DeepONet to preserve the physical relationships between relevant variables.

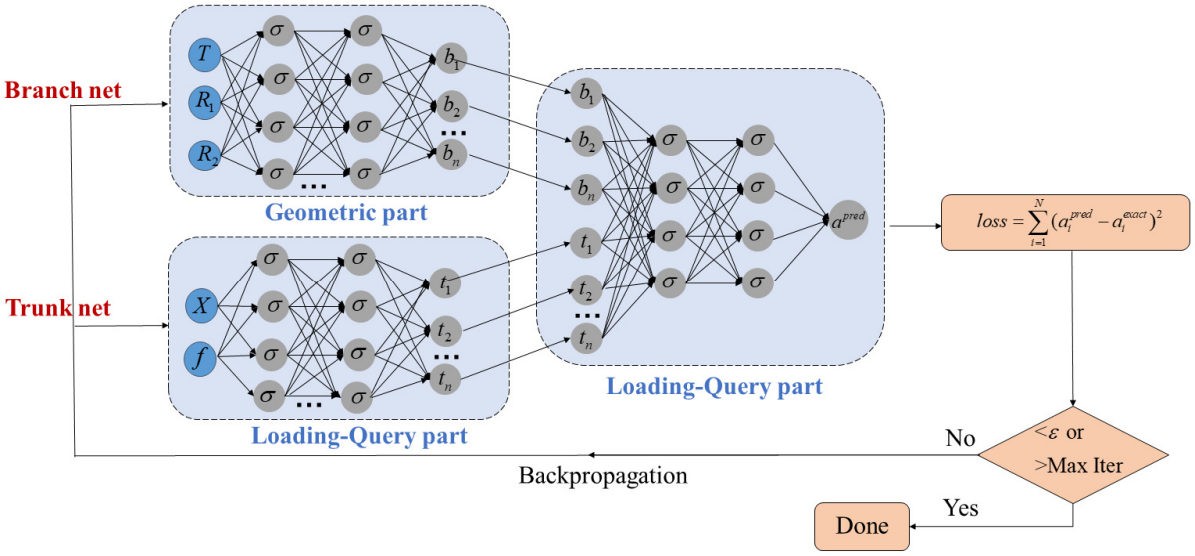



**Figure 4.** DeepONet framework proposed in this work.

It is important to note that in the classic DeepONet method, the outputs of the branch network and the trunk network are combined by a dot product operation followed by summation. Some scholars argue that there may be issues related to insufficient information exchange between the networks [27]. Related improvements include earlier or more complex methods of information exchange, among others. In the problem of predicting the explosive separation spectral acceleration addressed in this paper, considering the relatively small number of input variables in the branch network and the weaker independence among the related variables, it suggests the need for more interaction between the branch and trunk networks. Therefore, the DeepONet method proposed in this paper incorporates a neural network structure that facilitates further information exchange by merging the outputs of the branch and trunk networks through an additional network layer, as shown in Figure 4. This approach, while respecting the differences between the trunk and branch networks, aims to enhance the interaction between them, thereby improving the predictive performance.

### *3.2. Data Acquisition and Neural Network Configuration*

Both the detonation cord and bulkhead models are computed using Abaqus 2020. The detonation cord model requires calculation for a single condition, while the bulkhead model is processed in batch for 580 different conditions, facilitated by Python 3.8 scripts. The primary distinction between these conditions lies in the geometric parameters, specifically the bulkhead thickness, internal reinforcement parameter $r_1$, and external reinforcement parameter $r_2$, which are randomly selected within the following ranges: 10 mm to 20 mm for thickness, 40 mm to 120 mm for $r_1$, and 8 mm to 24 mm for $r_2$. After batch modeling, time-domain acceleration responses at six positions are exported and converted to frequency-domain responses using the shock response spectrum method. Spectral acceleration amplitudes are extracted at 10 frequency positions from 1000 Hz to 10,000 Hz, with a 1000 Hz interval. These spectral responses, along with geometric and spatial data, are saved, resulting in a four-dimensional dataset of size 580 × 6 × 10 × 6 (number of conditions, measurement points, frequencies, and input–output variables).

The DeepONet model is implemented using TensorFlow 1.15. The neural network consists of three parts, each with seven hidden layers, 60 neurons per layer, and a hyperbolic tangent (tanh) activation function. The model is initially trained for 10,000 iterations using the Adam optimizer, followed by fine-tuning with the L-BFGS method. The L-BFGS convergence criteria are set to a maximum of 10,000 iterations or when the error between consecutive iterations falls below a predefined threshold.

## 4. Results and Discussion

### *4.1. Typical Response of Cabin Structure in Explosive Separation Environment*

The energy generated during separation process is transmitted to the spacecraft structure in the form of shock waves [29]. The acceleration response of the cabin structure during the separation process is shown in Figure 5. In the initial stage, the acceleration load is transmitted upward along the bottom of the cabin in a ring-like pattern. At this point, a strong acceleration response is observed in the region ahead of the shock wave. Once the shock wave reaches the upper boundary, it reflects back and combines with the subsequent shock waves, forming a complex pattern throughout the structure.

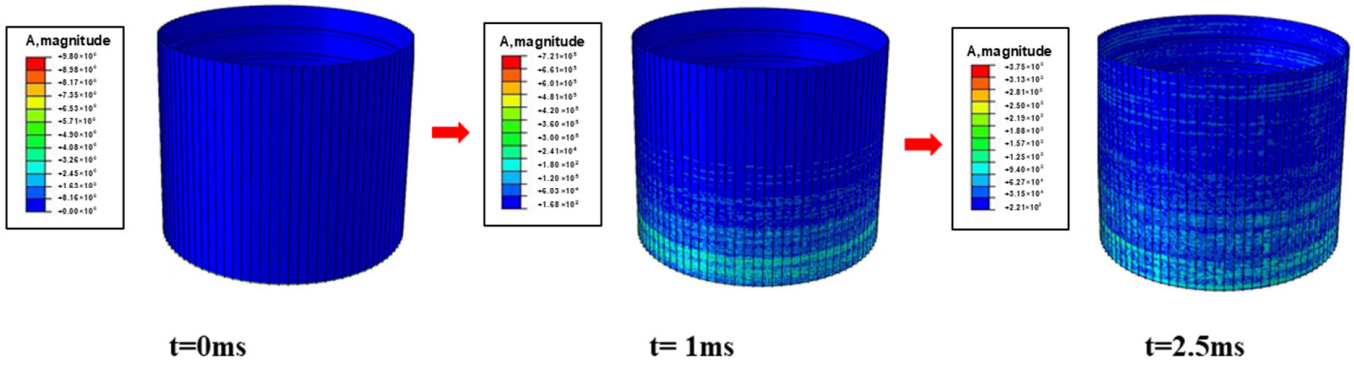



**Figure 5.** Acceleration response of the bulkhead.

Due to the complexity of the shock wave response curve after superposition, it is often converted to a spectral acceleration in the frequency domain for analysis [31,32]. It can also be observed that the shock wave primarily propagates along the axial direction, which produces the most significant shock response during the explosive separation process in practices. Therefore, after collecting the time-domain acceleration curves at each measurement point, the data are converted into a shock response spectrum in the 100–10,000 Hz range using a gain factor of 10, a 1/12 octave frequency interval, and a 100 k sampling rate. The peak values of the shock response spectrum curve within this frequency range are listed in Table 3 for typical measurement points in Figure 6a., and the shock response spectra for the relevant measurement points are shown in Figure 6b.

**Table 3.** Acceleration response spectra at typical measurement points on the bulkhead.

| Location | Explosion Source | P1 | P2 | P3 | P4 | P5 | P6 |
|---|---|---|---|---|---|---|---|
| Acceleration (g) | 48,200 | 19,890 | 8410 | 7650 | 6850 | 6480 | 4610 |

It is clear that the peak values of the shock response spectrum decrease most significantly between the explosion source and the spacecraft structure, as shown in Table 3, as well as in the initial stage of shock transmission along the ribbed structure, as shown in Figure 6. In the initial shock transmission stage, from the explosion source to measurement point P1, the shock wave travels approximately 0.7 m, and the maximum shock response spectrum value decreases from 19,890 g to 8410 g (where g = 9.8 m/s$^2$), representing a reduction of nearly 60%, indicating substantial attenuation of the shock environment. Between P1 and P5, where the shock wave travels about 2.4 m, the maximum value decreases by approximately 67%. However, between measurement P2 and P5, the shock environment only attenuates by about 23%. This demonstrates that the discontinuous interfaces along the shock transmission path significantly attenuate the shock. Additionally, the shock response spectra from 1000 Hz to 10,000 Hz, shown in Figure 6b, reveal that the spectral acceleration increases with the natural frequency in the range of 1000 Hz to 5000 Hz, with the peak spectral acceleration occurring between 5000 Hz and 10,000 Hz. This phenomenon will guide the design of the subsequent neural network.

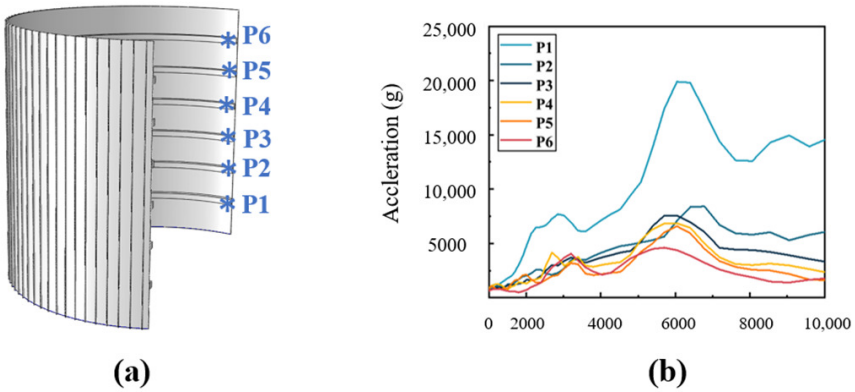



**Figure 6.** Location distribution (**a**) and responses (**b**) of typical measurement points.

### *4.2. DeepONet Prediction Results*

The final surrogate model was constructed using the neural network architecture described in Section 3.2, which consists of seven hidden layers and 60 neurons per layer—a configuration selected based on prior evaluations (with more detailed comparisons provided in Section 4.4). The model was trained using 10,000 iterations of the Adam optimizer, followed by further refinement with L-BFGS optimization. The prediction performance of the neural network is evaluated using the L2 error, that is

$$Error == \sqrt{\frac{\sum_{i=1}^{N}\left[ai^{pred} - ai^{exact}\right]^2}{\sum_{i=1}^{N} ai^{exact2}}} \tag{8}$$

where $ai^{pred}$ and $ai^{exact}$ are the $i$-th predicted value and the exact value, respectively. The resulting L2 error of the model is 5.65%, which is considered acceptable for engineering applications [11,12].

Furthermore, a scatter plot comparing the predicted and exact spectral acceleration responses across all test cases is shown in Figure 7. It can be observed that, except for a few outliers, the predictions closely match the true responses. This further confirms the accuracy and reliability of the DeepONet-based surrogate model.

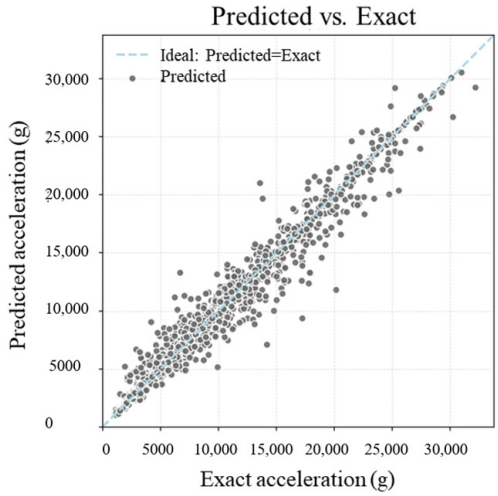



**Figure 7.** Comparison between predicted and exact responses on the test set.

### *4.3. Prediction Results on Typical Geometric Configurations*

Based on the prediction results in Section 4.2, we further present targeted comparisons between the finite element (FE) results and the neural network predictions for different geometric configurations, including variations in internal stiffeners, external stiffeners, and cabin wall thickness. As shown in Figures 8–10, these comparisons also serve as the basis for analyzing the influence of geometric changes on the spectral acceleration response of the spacecraft structure.

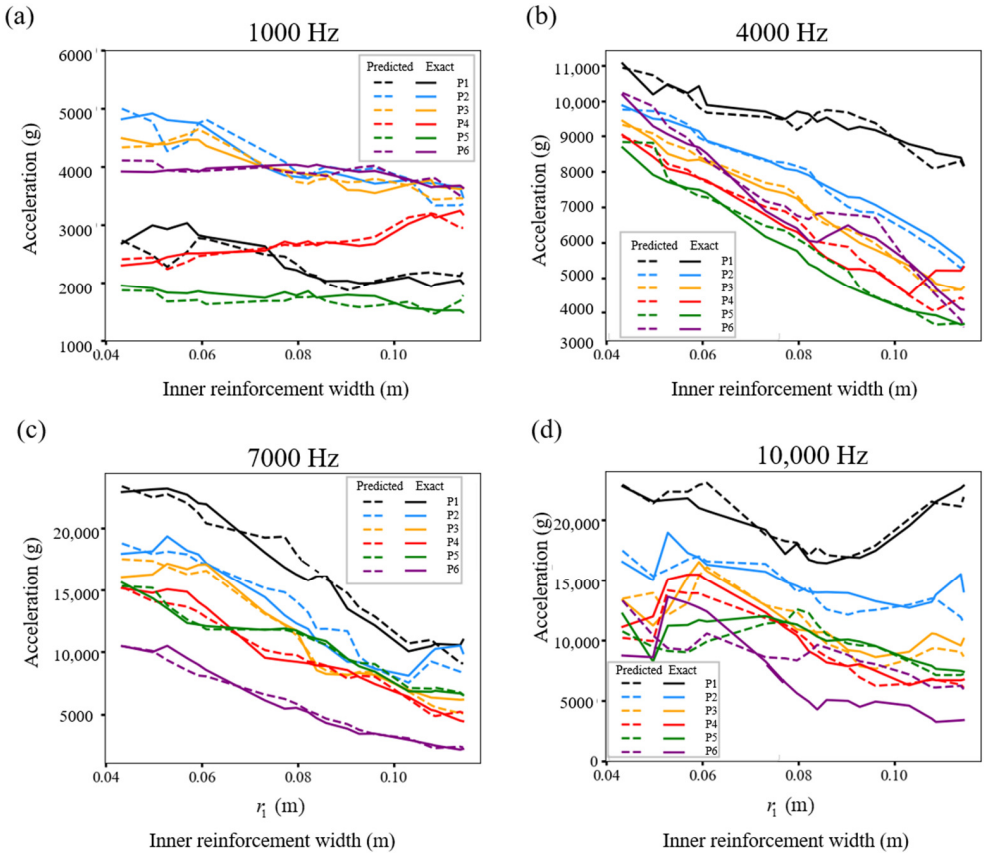



**Figure 8.** Amplitude of spectral acceleration response varies with inner reinforcement width at (**a**) 1000 Hz, (**b**) 4000 Hz, (**c**) 7000 Hz, and (**d**) 10,000 Hz.

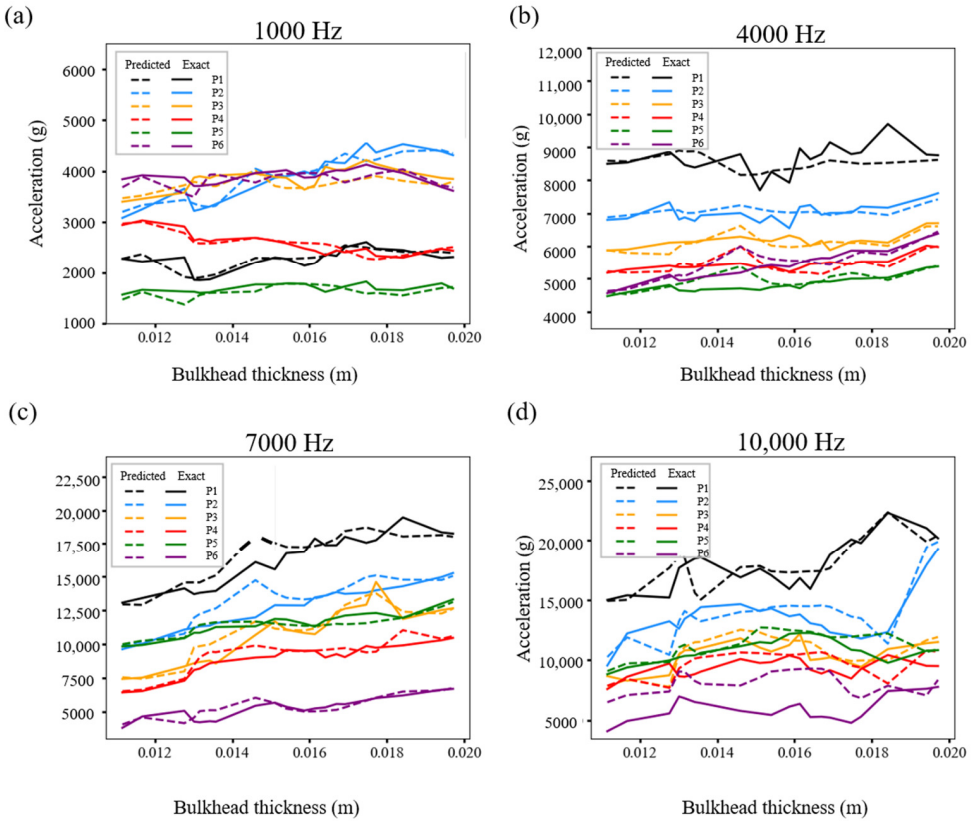



**Figure 9.** Amplitude of spectral acceleration response varies with bulkhead thickness at (**a**) 1000 Hz, (**b**) 4000 Hz, (**c**) 7000 Hz, and (**d**)10,000 Hz.

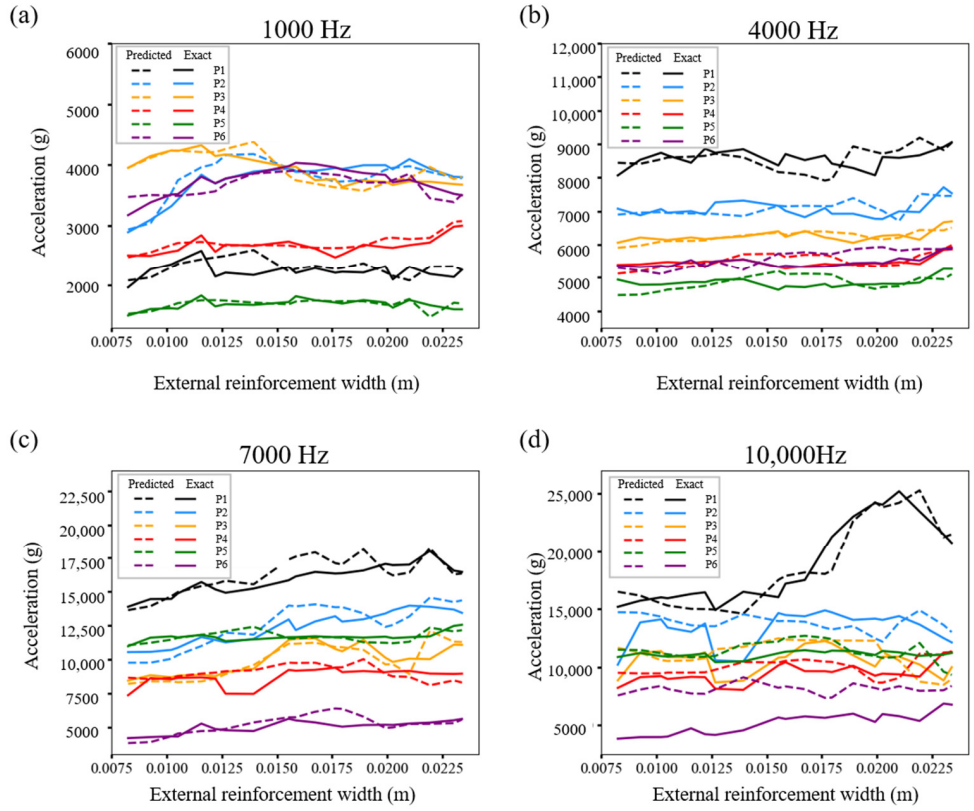



**Figure 10.** Amplitude of spectral acceleration response varies with external reinforcement width at (**a**) 1000 Hz, (**b**) 4000 Hz, (**c**) 7000 Hz, and (**d**) 10,000 Hz.

The acceleration response is largely determined by two dominant factors: the inertial mass of the responding component and the stiffness of the structure. Figure 8 illustrates the influence of the internal reinforcement width parameter on the shock environment. It is evident that increasing the width of the internal reinforcement significantly reduces the amplitude of the spectral acceleration response.

This can be attributed to the fact that the internal reinforcement is arranged circumferentially along the inner side of the bulkhead, perpendicular to the direction of shock wave propagation. Increasing the reinforcement width effectively increases the local inertial mass, which acts as a vibration absorber.

Moreover, this mass-damping effect is frequency-dependent—it is less pronounced at lower frequencies and becomes more significant in the high-frequency range. This also explains why the vibration suppression effect is not obvious at 1000 Hz, even when the internal reinforcement width is increased.

Figure 9 illustrates the influence of bulkhead thickness on the shock environment. It can be observed that increasing the bulkhead thickness has a limited effect on the shock response, and in certain frequency bands, the spectral acceleration response even increases. This is because the cabin wall is a continuous structure that primarily acts as a wave transmission channel, rather than spaced reinforcement. Increasing its thickness raises both mass and stiffness; however, the increase in stiffness (which, in the case of bending waves, is proportional to the cube of the thickness) far exceeds the linear increase in mass. As a result, the natural frequency rises, leading to a greater acceleration response.

The effect of external reinforcement width on the shock environment is shown in Figure 10. It can be observed that, except for a few measurement points, the external reinforcement width has a minimal impact on the shock environment. This is because it is aligned along the axial direction of the wall—parallel to the wave propagation direction—and does not significantly interrupt the transmission path or provide localized mass. Moreover, its scale (mass and stiffness) is relatively small compared to the cabin wall itself. Hence, its effect on the spectral acceleration response is minimal.

Finally, by combining Figures 8–10, it can be observed that increasing the width of the internal stiffeners has the most significant effect in reducing the spectral acceleration response of the cabin structure, due to its relatively high mass-induced damping effect. In contrast, the influence of external stiffeners is less pronounced. Moreover, increasing the cabin wall thickness may slightly increase the spectral acceleration response, as it enhances structural stiffness and provides a broader wave transmission path, rather than introducing mass damping. From a design perspective, these findings suggest that increasing the width of internal stiffeners—especially those located near the cabin wall—can effectively reduce the spectral acceleration response during explosive separation events. Additionally, the proposed DeepONet method demonstrates good predictive accuracy for the spectral acceleration response of the structure. Further discussions on the neural network design and performance can be found in Sections 4.4–4.7.

### *4.4. Parameter Analysis of Neural Network*

Considering that DeepONet in this study is composed of three interconnected parts, its neural network complexity is higher compared to traditional fully connected neural networks. As the neural network structure is crucial to the prediction results, we analyze the impact of neural network parameters on the prediction accuracy, specifically focusing on the influence of the number of layers and the number of neurons per layer. We examine the prediction errors of DeepONet with six different numbers of layers (3, 4, 5, 6, 7, 8) and five different numbers of neurons (20, 40, 60, 80, 100), as shown in Table 4. It should be noted that the error here is L2 error in Equation (8). Meanwhile, when the network has three

layers, this means that the branch network, trunk network, and information interaction parts each have three layers. It can be observed that the prediction errors are generally within 9%, with many configurations showing errors between 6% and 7%. The optimal configuration provided yields a prediction error of 5.65%.

**Table 4.** Prediction errors with different layer numbers and neuron numbers by DeepONet.

| Neurons \ Layers | 3 | 4 | 5 | 6 | 7 | 8 |
|---|---|---|---|---|---|---|
| 20 | 8.43% | 8.63% | 8.15% | 7.54% | 7.44% | 7.61% |
| 40 | 6.72% | 6.89% | 7.54% | 7.76% | 6.34% | 6.62% |
| 60 | 7.36% | 7.07% | 7.16% | 6.56% | 5.65% | 6.18% |
| 80 | 6.92% | 6.1% | 6.27% | 6.96% | 5.81% | 6.21% |
| 100 | 6.44% | 5.86% | 6.09% | 6.04% | 8.61% | 8.30% |

While we record the prediction error of different configurations, we also track the evolution of the loss function. Here, four representative loss function evolution plots are provided: the shallowest and narrowest configuration with three layers and 20 neurons (denoted by the light blue dashed line, L3N20), the deeper and narrower configuration with seven layers and 60 neurons (denoted by the solid green line, L7N60), the shallower and wider configuration with four layers and 100 neurons (denoted by the orange dotted line, L4N100), and the deepest and widest configuration with eight layers and 100 neurons (denoted by the red line, L8N100). Figure 11 shows the loss function evolution throughout the entire training process and the behavior just before convergence, respectively.

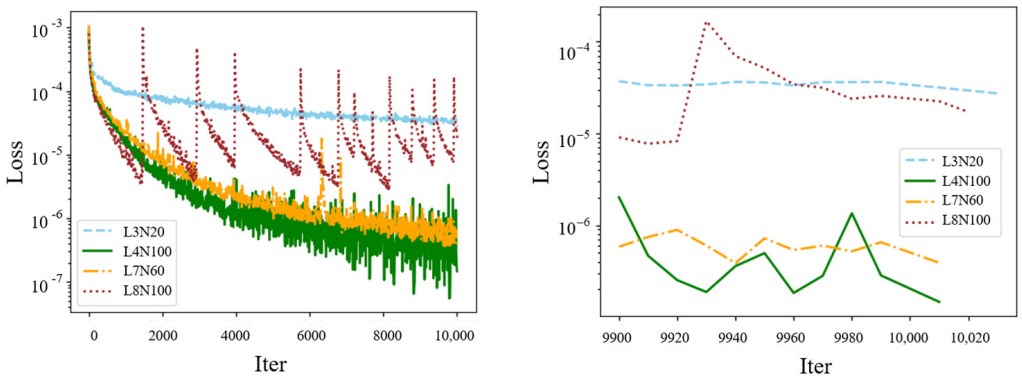



**Figure 11.** (**a**) Global loss function evolution and (**b**) loss function evolution.

The vertical axis "loss" represents the normalized mean squared error (NMSE), defined as follows:

$$Loss == \frac{1}{N}\sum_{i=1}^{N}\left[a_{traini}^{pred} - a_{traini}^{exact}\right]^2 \quad (9)$$

where $a_{traini}^{pred}$ and $a_{traini}^{exact}$ denote the $i$-th normalized predicted values and the normalized ground truth values in the training dataset, respectively. "Epoch" refers to the number of iterations during the training process. From the perspective of training speed, the green and red curves, which represent the configurations with the most neurons per layer, show the fastest decrease in the loss function. In other words, wider neural networks tend to have faster training speeds in the early stages. This could be because the wider and deeper network, with more neurons in each layer, is better at approximating complex functional relationships. However, in terms of training stability, the blue and orange curves, which

represent networks with fewer neurons, exhibit the smallest fluctuations in the loss function. This may be because a smaller number of neurons leads to a smaller search space for global training parameters, making the loss function more stable. The depth (number of layers) and the width (number of neurons) together influence the complexity of the neural network structure. A narrower and shallower network is prone to underfitting, as shown by L3N20 in Figure 11. On the other hand, a very deep and wide neural network, such as L8N100, although it provides greater fitting capacity, is more likely to overfit [33,34].

An illustrative example is the green curve of L4N100, which achieved strong performance during training, with a low loss and a training error of only 0.51%, outperforming L7N40, which had the best test set performance and a training error of 0.76%. However, its test set predictions were suboptimal. This can be attributed to the wider neural network's greater number of trainable parameters per layer, enabling better approximation of complex input–output mappings during training but also increasing the risk of overfitting, leading to superior training set performance but poorer generalization to the test set. Such an overly wide neural network configuration leads the model to excessively learn individual characteristics in the training set, resulting in poor performance when applied to the test set or to new, unseen datasets for prediction.

### *4.5. Why DeepONet*

#### 4.5.1. Comparison with the Finite Element Method

All finite element simulations and neural network training were conducted on a personal Lenovo desktop equipped with an 8-core Intel i5 processor and a GTX 1050Ti GPU. For each loading case, the FEM required approximately 57 min of computation time. In contrast, after an offline training phase of approximately 5 min, the DeepONet model required only 17 s to predict all 60 cases in the test set. Compared to FEM, DeepONet achieved a computational efficiency improvement of more than four orders of magnitude. This dramatic acceleration is particularly beneficial for large-scale applications, such as optimization design of spacecraft structures, where numerous evaluations are required.

#### 4.5.2. Comparison with Conventional Neural Networks

Fully Connected Neural Network (FNN)

To compare the prediction accuracy of DeepONet with that of conventional neural networks, we also conducted training and prediction using a FNN. A total of 30 different network configurations were tested, with the number of neurons per layer ranging from 20 to 100, and the number of hidden layers varying from 4 to 14. (Due to the simpler architecture of FNNs, a larger number of hidden layers was explored in the numerical experiments.) The prediction results are summarized in Table 5.

**Table 5.** Prediction errors with different layer numbers and neuron numbers by FNN.

| Neurons \ Layers | 4 | 6 | 8 | 10 | 12 | 14 |
|---|---|---|---|---|---|---|
| 20 | 10.11% | 11.6%% | 9.72% | 9.36% | 9.44% | 8.85% |
| 40 | 9.75% | 10.99% | 8.63% | 9.03% | 7.30% | 8.27% |
| 60 | 9.26% | 7.61% | 6.89% | 7.77% | 6.77% | 6.79% |
| 80 | 10.52% | 8.25% | 6.38% | 6.85% | 6.06% | 6.78% |
| 100 | 8.56% | 7.55% | 6.08% | 6.04% | 6.16% | 6.16% |

As shown in Table 5, the lowest prediction error achieved by FNN is 6.04%, which is higher than the minimum error of 5.65% attained by DeepONet. However, the performance gap between the two methods goes beyond just the minimum error. To gain a more intuitive understanding, we conducted a comprehensive comparison by evaluating both DeepONet and FNN under 30 different neural network configurations (Figure 12). The results demonstrate that DeepONet consistently outperforms FNN, even without extensive hyperparameter tuning. After optimization, DeepONet achieved prediction errors within the 5–6% range in three configurations, while the best-performing FNN configuration still resulted in errors exceeding 6%. These findings indicate that DeepONet surpasses FNN not only in its best-case performance but also in its overall robustness and general predictive capability.

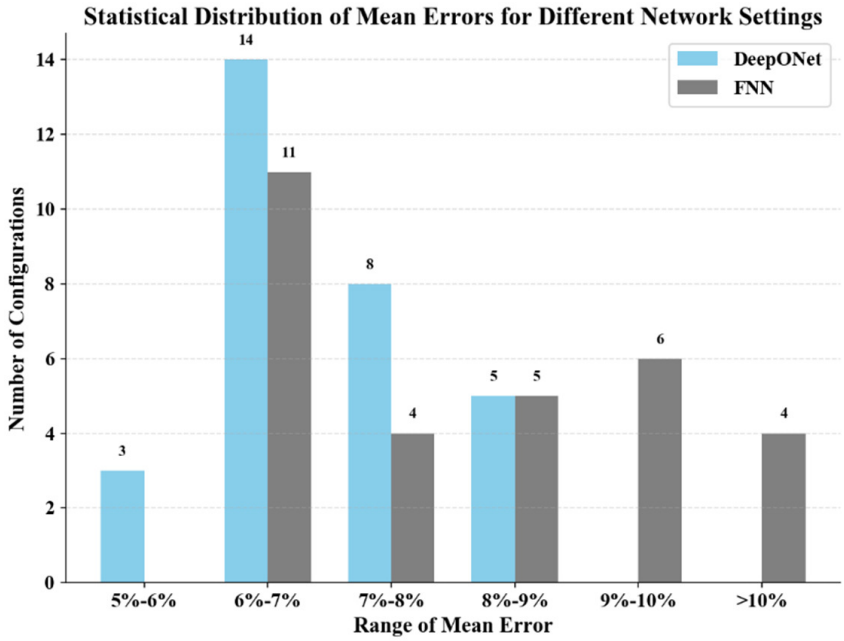



**Figure 12.** Summary of L2 errors for DeepONet and FNN across 30 neural network parameter settings.

PINNs

PINNs embed physical laws into neural networks by enforcing PDEs and boundary conditions. However, for complex engineering structures, such as the spacecraft cabin segment studied here, the irregular geometry and intricate boundary conditions pose significant challenges for the effective application of PINNs. Additionally, since each working condition corresponds to a different geometry, the boundary conditions in PINNs must be redefined for every case. As a result, each PINN model is typically specialized for a single geometric configuration, limiting its generalization. In contrast, DeepONet does not rely on explicit physical constraints. Instead, it encodes geometry as part of the input and learns an operator that maps geometric variations to the corresponding physical responses. Therefore, for similar problems, the DeepONet approach is generally more suitable than the PINN method.

### *4.6. Generalization Analysis*

To demonstrate the generalization capability of the DeepONet method—namely, its ability to make accurate predictions beyond the training data range—we retrained the neural network model using the previously identified optimal configuration of seven layers with 60 neurons each.

Given that internal reinforcement has the greatest influence on the structural response, we conducted the generalization analysis by varying the data size and range related to the internal reinforcement. Specifically, in the original model, the internal reinforcement width ranged from 40 mm to 120 mm, with both training and testing data sampled within this full range.

In the generalization test model, however, the network was trained only on cases with internal reinforcement widths ranging from 40 mm to 110 mm, and tested on unseen cases in the 110–120 mm range. The corresponding prediction results under this extrapolation scenario are shown as red scatter points in Figure 13.

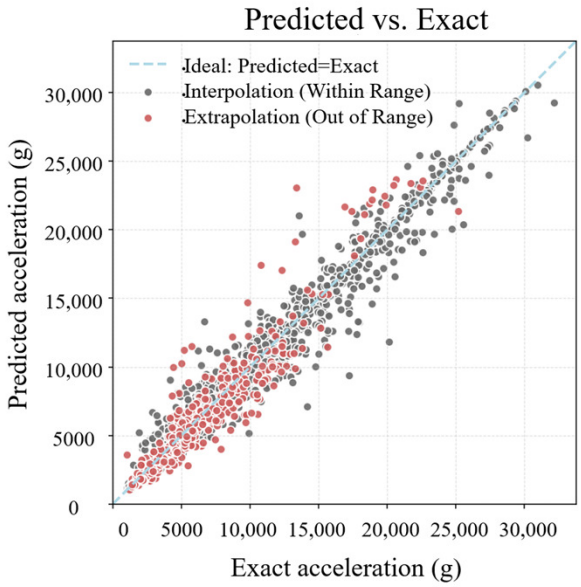



**Figure 13.** Comparison of machine learning prediction errors between interpolation and extrapolation regions for internal reinforcement parameters.

Compared to the interpolation case in Figure 7—where both the training and testing data were within the full 40–120 mm range (gray points in Figure 13)—the extrapolation case (red points), in which the model was trained on 40–110 mm and tested on 110–120 mm, still yields accurate predictions. This demonstrates the strong generalization capability of the DeepONet method.

### *4.7. Impact of the Data Frequency Band Range in Frequency Domain Machine Learning*

In previous analysis, we observed that the spectral acceleration response exhibits a more complex variation within the 5000–10,000 Hz range compared to the 1000–5000 Hz range. Meanwhile, in Section 4.3 (Figures 8–10), we found that DeepONet does not perform well in predicting the high-frequency response at 10,000 Hz. In practical engineering applications, the primary focus is typically on the maximum spectral acceleration response amplitude across the entire natural frequency range.

To analyze in detail the underlying reasons for the poor prediction at high frequencies, we define the data from 1000 to 5000 Hz as mid-frequency data and the data from 5000 to 10,000 Hz as high-frequency data. An intuitive hypothesis is that the patterns in mid-frequency data are relatively simple, while those in high-frequency data are more complex. Since neural network optimization follows the principle of global error minimization, it is possible that the network places more emphasis on learning the simpler, more easily fitted patterns in the mid-frequency data, resulting in insufficient training for the more crucial high-frequency data. That is, in our frequency-domain machine learning model for predicting the amplitude of spectral acceleration response of spacecraft, the learning

space of the data may affect the final result. To validate this hypothesis, we performed an additional set of calculations, where we excluded the mid-frequency data and focused solely on learning and predicting the high-frequency data in the 5000–10,000 Hz range. The prediction results are shown in Table 6.

**Table 6.** DeepONet high-frequency prediction results.

| Neurons \ Layers | 3 | 4 | 5 | 6 | 7 | 8 |
|---|---|---|---|---|---|---|
| 20 | 9.38% | 8.24% | 7.13% | 8.07% | 7.27% | 7.6% |
| 40 | 8.52% | 5.83% | 6.09% | 6.12% | 4.76% | 6.08% |
| 60 | 7.06% | 7.07% | 5.40% | 6.56% | 6.10% | 5.18% |
| 80 | 5.52% | 5.37% | 5.51% | 5.75% | 5.16% | 6.74% |
| 100 | 5.5% | 5.00% | 5.11% | 6.64% | 5.65% | 6.76% |

It can be observed that when only high-frequency data are employed, the minimum error is 4.76% with seven layers and 40 neurons, which is about 10% lower than the minimum error of 5.65% (the best setting L7N60 in Section 4.4) when both mid- and high-frequency data are predicted. A more significant difference is seen in the prediction results for specific frequency bands. As shown in Figure 14, when predicting the high-frequency response at 10,000 Hz, the prediction results using only high-frequency data (blue curve) are clearly superior to those using combined mid- and high-frequency data (red dashed line). This is because the patterns in mid-frequency data are relatively simple, while those in high-frequency data are more complex. The neural network learns different input–output mappings depending on the data. When both mid- and high-frequency data are used for training, the network tends to approximate the simpler mappings of the mid-frequency data, which leads to insufficient learning of the more informative high-frequency data and results in poorer high-frequency prediction performance. This validates the effectiveness of learning data frequency band range in the frequency domain machine learning model for explosive separation.

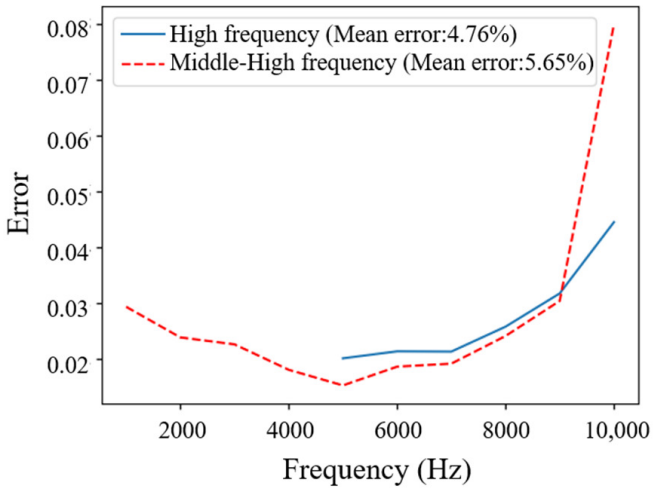



**Figure 14.** Prediction errors for each frequency band in the high-frequency space and mid–high-frequency space.

## 5. Conclusions

This work proposes a high-frequency spectral acceleration response prediction method for a spacecraft based on DeepONet. The method preserves the physical relationships between the input variables in the explosive separation problem. By establishing a neural network surrogate model, the influence of spacecraft geometric structural parameters on the explosive separation shock environment is analyzed, and the influence of the neural network architecture and dataset space on the prediction results is also examined. The main conclusions are as follows:

(i) The internal reinforcement structure plays a significant role in suppressing the maximum spectral acceleration response inside the spacecraft during explosive separation. The dimensions of the external reinforcement and the wall thickness have minimal influence, and in some frequency ranges, the presence of external reinforcements even amplifies the maximum spectral acceleration inside the spacecraft. In the structural design of explosive separation spacecraft, emphasis should be placed on strengthening the inner reinforcement width near the explosive element position.

(ii) The proposed DeepONet can achieve relatively good prediction of spectral acceleration responses. Meanwhile, a wider neural network results in faster training but is more prone to overfitting.

(iii) In explosive separation frequency-domain machine learning, the learning space of frequency-domain data will affect the prediction results. Learning and predicting the complex but crucial high-frequency data alone leads to better prediction results than simultaneously learning some simple yet useless mid- and high-frequency data.

It should be noted that, considering the high cost of using a full-scale cabin model, the surrogate model developed in this study is based on simulation data. In future work, we plan to integrate this surrogate model with optimization algorithms such as genetic algorithms to perform inverse structural design and optimization, and the designed structures will be experimentally validated to achieve cabin structures with excellent shock resistance. Therefore, the method proposed in this study can also serve as an effective early-stage evaluation tool prior to conducting large-scale physical tests. This is particularly valuable for the rapid structural design and evaluation process in aerospace engineering.

**Author Contributions:** Methodology, X.C. and X.K.; Software, X.C. and Y.W.; Formal analysis, Z.Q.; Investigation, X.C. and G.C.; Resources, Z.C.; Data curation, Y.W.; Writing—original draft, X.C.; Writing—review & editing, Z.C. and G.C.; Project administration, Z.Q. and Y.L.; Funding acquisition, Y.L. and X.K. All authors have read and agreed to the published version of the manuscript.

**Funding:** This research received no external funding.

**Data Availability Statement:** The raw data supporting the conclusions of this article will be made available by the authors on request.

**Acknowledgments:** During the preparation of this work the authors used ChatGPT 4o for language polishing. After using this tool, the authors reviewed and edited the content as needed and take full responsibility for the content of the publication.

**Conflicts of Interest:** The authors declare no conflict of interest.

## References

1. Huang, W.; Rong, W.; Liu, D.; Jiang, C.; Jia, H.; Bao, J.; Fang, J. Design and realization of recovery system of chang'e-5 reentry spacecraft. *Space Sci. Technol.* **2021**, *2021*, 9898756. [CrossRef]
2. Tanzman, J.R. Material consideration in the STEREO solar array design. *Acta Astronaut.* **2018**, *63*, 1239–1245. [CrossRef]
3. Morais, O.M.F.; Vasques, C.M.A. Shock environment design for space equipment testing. *Proc. Inst. Mech. Eng. Part G J. Aerosp. Eng.* **2017**, *231*, 1154–1167. [CrossRef]

4. Qi, G.O.N.G.; Zhang, J.; Chunlin, T.; Cancan, W.A.N.G. Neural networks combined with importance sampling techniques for reliability evaluation of explosive initiating device. *Chin. J. Aeronaut.* **2012**, *25*, 208–215.
5. Zhao, H.; Liu, W.; Ding, J.; Sun, Y.; Li, X.; Liu, Y. Numerical study on separation shock characteristics of pyrotechnic separation nuts. *Acta Astronaut.* **2018**, *151*, 893–903. [CrossRef]
6. Brunton, S.L.; Noack, B.R.; Koumoutsakos, P. Machine learning for fluid mechanics. *Annu. Rev. Fluid Mech.* **2020**, *52*, 477–508. [CrossRef]
7. Liu, X.; Athanasiou, C.E.; Padture, N.P.; Sheldon, B.W.; Gao, H. A machine learning approach to fracture mechanics problems. *Acta Mater.* **2020**, *190*, 105–112. [CrossRef]
8. Guo, K.; Yang, Z.; Yu, C.H.; Buehler, M.J. Artificial intelligence and machine learning in design of mechanical materials. *Mater. Horiz.* **2021**, *8*, 1153–1172. [CrossRef]
9. Guo, S.; Huang, J.; Qian, W.; Liu, J.; Zhu, W.; Zhang, C. Discovery of high energy and stable prismane derivatives by the high-throughput computation and machine learning combined strategy. *FirePhysChem* **2024**, *4*, 55–62. [CrossRef]
10. Morris, C.; Yang, J. Understanding Multi-Vehicle Collision Patterns on Freeways—A Machine Learning Approach. *Infrastructures* **2020**, *5*, 62. [CrossRef]
11. Kong, X.S.; Gao, H.; Jin, Z.; Zheng, C.; Wang, Y. Predictions of the responses of stiffened plates subjected to underwater explosion based on machine learning. *Ocean Eng.* **2023**, *283*, 115216. [CrossRef]
12. He, Z.; Chen, X.; Zhang, X.; Jiang, Y.; Ren, X.; Li, Y. Damage prediction of hull structure under near-field underwater explosion based on machine learning. *Appl. Ocean. Res.* **2025**, *154*, 104329. [CrossRef]
13. Wang, Y.; Zeng, Q.; Wang, J.; Li, Y.; Fang, D. Inverse design of shell-based mechanical metamaterial with customized loading curves based on machine learning and genetic algorithm. *Comput. Methods Appl. Mech. Eng.* **2022**, *401*, 115571. [CrossRef]
14. Masi, F.; Stefanou, I.; Vannucci, P.; Maffi-Berthier, V. Thermodynamics-based artificial neural networks for constitutive modeling. *J. Mech. Phys. Solids* **2021**, *147*, 104277. [CrossRef]
15. Raissi, M.; Perdikaris, P.; Karniadakis, G.E. Physics-informed neural networks: A deep learning framework for solving forward and inverse problems involving nonlinear partial differential equations. *J. Comput. Phys.* **2019**, *378*, 686–707. [CrossRef]
16. Karniadakis, G.E.; Kevrekidis, I.G.; Lu, L.; Perdikaris, P.; Wang, S.; Yang, L. Physics-informed machine learning. *Nat. Rev. Phys.* **2021**, *3*, 422–440. [CrossRef]
17. Rao, C.; Sun, H.; Liu, Y. Physics-informed deep learning for computational elastodynamics without labeled data. *J. Eng. Mech.* **2021**, *147*, 04021043. [CrossRef]
18. Alzubaidi, L.; Bai, J.; Al-Sabaawi, A. A survey on deep learning tools dealing with data scarcity: Definitions, challenges, solutions, tips, and applications. *J. Big Data* **2023**, *10*, 46. [CrossRef]
19. Hua, N.; Lu, W. Basis operator network: A neural network-based model for learning nonlinear operators via neural basis. *Neural Netw.* **2023**, *164*, 21–37. [CrossRef]
20. Li, Z.; Kovachki, N.; Azizzadenesheli, K.; Liu, B.; Bhattacharya, K.; Stuart, A.; Anandkumar, A. Fourier neural operator for parametric partial differential equations. *arXiv* **2020**, arXiv:2010.08895.
21. Lu, L.; Jin, P.; Pang, G.; Zhang, Z.; Karniadakis, G.E. Learning nonlinear operators via DeepONet based on the universal approximation theorem of operators. *Nat. Mach. Intell.* **2021**, *3*, 218–229. [CrossRef]
22. Mao, Z.; Lu, L.; Marxen, O.; Zaki, T.A.; Karniadakis, G.E. DeepM&Mnet for hypersonics: Predicting the coupled flow and finite-rate chemistry behind a normal shock using neural-network approximation of operators. *J. Comput. Phys.* **2021**, *447*, 110698.
23. Goswami, S.; Yin, M.; Yu, Y.; Karniadakis, G.E. A physics-informed variational DeepONet for predicting crack path in quasi-brittle materials. *Comput. Methods Appl. Mech. Eng.* **2022**, *391*, 114587. [CrossRef]
24. Huang, M.; Liu, C.; Guo, Y.; Zhang, L.; Du, Z.; Guo, X. A mechanics-based data-free Problem Independent Machine Learning (PIML) model for large-scale structural analysis and design optimization. *J. Mech. Phys. Solids* **2024**, *193*, 105893. [CrossRef]
25. Tan, L.; Chen, L. Enhanced deeponet for modeling partial differential operators considering multiple input functions. *arXiv* **2022**, arXiv:2202.08942.
26. Wang, S.; Wang, H.; Perdikaris, P. Improved architectures and training algorithms for deep operator networks. *J. Sci. Comput.* **2022**, *92*, 35. [CrossRef]
27. He, J.; Koric, S.; Kushwaha, S.; Park, J.; Abueidda, D.; Jasiuk, I. Novel DeepONet architecture to predict stresses in elastoplastic structures with variable complex geometries and loads. *Comput. Methods Appl. Mech. Eng.* **2023**, *415*, 116277. [CrossRef]
28. Salvador, M.; Marsden, A.L. Branched latent neural maps. *Comput. Methods Appl. Mech. Eng.* **2024**, *418*, 116499. [CrossRef]
29. Wang, Y.; Kang, X.; Feng, L.; Li, Y. Design and characterization of a pyroshock reduction structure based on local resonance mechanisms. *Aerosp. Sci. Technol.* **2024**, *151*, 109262. [CrossRef]
30. Jiang, Y.; Yuan, H.; Li, Y.; Gao, R.; Li, Y. Damage boundary spectrum of pelvis-lumbar spine of seated human under vertical wide-band shock environment. *Int. J. Impact Eng.* **2023**, *182*, 104767. [CrossRef]
31. Li, B.W.; Li, Q.M. Damage boundary of structural components under shock environment. *Int. J. Impact Eng.* **2018**, *118*, 67–77. [CrossRef]

32. Liu, Y.; Chen, Y.; Ding, B. Deep learning in frequency domain for inverse identification of nonhomogeneous material properties. *J. Mech. Phys. Solids* **2022**, *168*, 105043. [CrossRef]
33. Bejani, M.M.; Ghatee, M. A systematic review on overfitting control in shallow and deep neural networks. *Artif. Intell. Rev.* **2021**, *54*, 6391–6438. [CrossRef]
34. Li, H.; Rajbahadur, G.K.; Lin, D.; Bezemer, C.P.; Jiang, Z.M. Keeping deep learning models in check: A history-based approach to mitigate overfitting. *IEEE Access* **2024**, *12*, 70676–70689. [CrossRef]

**Disclaimer/Publisher's Note:** The statements, opinions and data contained in all publications are solely those of the individual author(s) and contributor(s) and not of MDPI and/or the editor(s). MDPI and/or the editor(s) disclaim responsibility for any injury to people or property resulting from any ideas, methods, instructions or products referred to in the content.